

A Constitutive Model of Soft Tissue: From Nanoscale Collagen to Tissue Continuum

HUANG TANG,¹ MARKUS J. BUEHLER,² and BRIAN MORAN^{1,3}

¹Department of Civil and Environmental Engineering, Northwestern University, 2145 Sheridan Road, Evanston, IL 60208-3109, USA; ²Laboratory for Atomistic and Molecular Mechanics, Department of Civil and Environmental Engineering, Massachusetts Institute of Technology, 77 Massachusetts Ave., Room 1-235A&B, Cambridge, MA, USA; and ³Present Address: King Abdullah University of Science and Technology (KAUST), Thuwal, Saudi Arabia

(Received 9 July 2008; accepted 16 March 2009; published online 8 April 2009)

Abstract—Soft collagenous tissue features many hierarchies of structure, starting from tropocollagen molecules that form fibrils, and proceeding to a bundle of fibrils that form fibers. Here we report the development of an atomistically informed continuum model of collagenous tissue. Results from full atomistic and molecular modeling are linked with a continuum theory of a fiber-reinforced composite, handshaking the fibril scale to the fiber and continuum scale in a hierarchical multi-scale simulation approach. Our model enables us to study the continuum-level response of the tissue as a function of cross-link density, making a link between nanoscale collagen features and material properties at larger tissue scales. The results illustrate a strong dependence of the continuum response as a function of nanoscopic structural features, providing evidence for the notion that the molecular basis for protein materials is important in defining their larger-scale mechanical properties.

Keywords—Multi-scale model, Collagen, Soft tissue, Molecular mechanics, Continuum, Finite element, Deformation, Failure, Mechanical properties.

INTRODUCTION

Soft tissue has many hierarchies of structure,^{1,8} starting from tropocollagen molecules that form fibrils, and proceeding to a bundle of fibrils that form fibers. The soft tissue is essentially a fiber-reinforced composite, while the fiber is a fibril-reinforced composite at smaller length scales. The overall mechanical behavior of the soft tissue depends on its hierarchically organized structure. A better understanding of the structure mechanisms controlling the mechanical behavior of soft tissue can play significant roles in tissue engineering. One of goals of

tissue engineering is to produce functional replacement tissue for clinical use.¹⁹ An example on the application of tissue engineering is the replacement or repair of an injured ligament or tendon due to overstretching, which requires an improved understanding of the structure-controlled mechanical behavior of soft tissue.

A physically motivated constitutive model is important to help better understand the structure-controlled deformation mechanisms of soft tissues. There exist a number of constitutive models of soft tissue, most of which^{12,15,20,24} account only for the tissue deformation in an elastic domain on the basis of hyperelasticity. In Kroon and Holzapfel,¹⁶ an anisotropic strain-energy function was used to develop the constitutive relations of a multiple collagen layers. The deformation behavior of soft tissue beyond physiological range of loading is characterized by irreversible deformation or damage. A complete constitutive model needs to account for the mechanisms controlling the irreversible deformation of soft tissue. Inelastic deformation of soft tissues was included in the modeling of arteries by Tanaka and Yamada²¹ and Tanaka *et al.*²² by means of a viscoplastic formulation. A rate-independent elastic–plastic model was used by Gasser and Holzapfel¹⁰ to simulate the constitutive behavior of fiber-reinforced biological soft tissue. Other studies focused on the development of a constitutive model of the posterior cruciate ligament.¹⁷

In this study, we propose a multi-scale constitutive model which takes material properties at different structural hierarchies of soft tissue into account through a hierarchical multi-scale coupling scheme. The model incorporates the deformation mechanisms of fibrils on the nanoscale into a macroscopic description of the constitutive behavior of tissue continuum. Here the irreversible deformation of soft tissue is mainly attributed to inelastic deformation occurring in the fibrils. The mechanical behavior of fibrils is modeled through molecular dynamics simulations

Address correspondence to Markus J. Buehler, Laboratory for Atomistic and Molecular Mechanics, Department of Civil and Environmental Engineering, Massachusetts Institute of Technology, 77 Massachusetts Ave., Room 1-235A&B, Cambridge, MA, USA. Electronic mail: mbuehler@MIT.EDU

(MD). The analysis reported here draws on earlier atomistic and molecular dynamics simulation results that provide a quantitative description of the mechanical behavior of collagen fibrils.^{3,4} By means of the multi-scale constitutive model, the physical mechanisms controlling the elastic–inelastic deformation of soft tissue are accounted for by means of hierarchical parameter passing. The major objective of this study is to shed lights on the correlation of molecular structure of soft tissue and its macroscopic mechanical behavior.

CONSTITUTIVE RELATIONS OF TISSUE CONTINUUM

Kinematics of Deformation for Tissue with Hierarchically Organized Structure

The hierarchical features of soft tissue are illustrated in Fig. 1. The fibrils are aligned with the fiber axis. The fibers have a parallel arrangement in the tissue. In the calculations conducted here, the tissue is treated as a homogenized continuum. Each material point in the continuum represents the overall response of a statistically homogeneous representative volume element (RVE) of the tissue. The deformation gradient is defined by $\bar{F}(\bar{X}, t) = \partial\chi(\bar{X}, t)/\partial\bar{X}$, where \bar{X} is a material point defined in the reference configuration Ω_0 , and $\bar{x} = \chi(\bar{X}, t)$ is the corresponding position in the current configuration Ω_t at time t . In Fig. 2, the multiplicative decomposition of the macroscopic deformation gradient of the RVE, \bar{F} , is described. The macroscopic deformation gradient \bar{F} can be understood as the volume average of the deformation gradient over the RVE subjected to homogeneous or periodic boundary conditions. As shown in the figure, the deformation gradient is multiplicatively decomposed as¹²

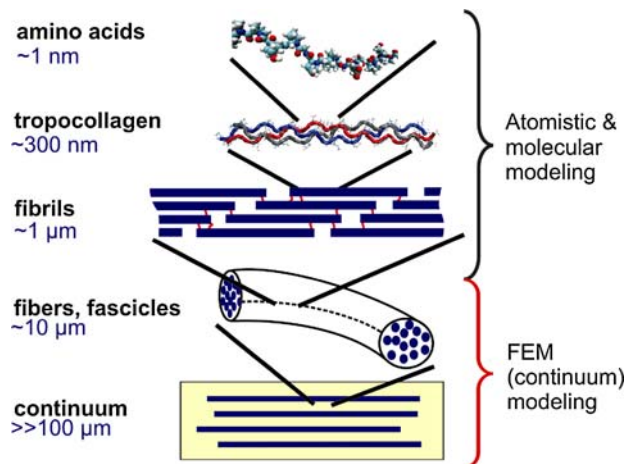


FIGURE 1. Schematic view of the Hierarchical features of tissue.

$$\bar{F} = \bar{F}_s \bar{F}_f, \tag{1}$$

where \bar{F}_f corresponds to a macroscopic uniaxial deformation along the fiber direction, and \bar{F}_s involves the remaining macroscopic shear deformation and rigid body rotation. For the case that all components in the tissue including fibrils, fibers and matrix materials are incompressible, it is shown that the uniaxial deformation along the fiber direction is uniform through the tissue RVE. Thus, we have

$$F_f = \bar{F}_f, \tag{2}$$

where F_f represents the local uniaxial deformation gradient. By uniaxial deformation, we mean the deformation associates with a state of uniaxial stress with \bar{F}_f written as

$$\begin{aligned} \bar{F}_f &= \bar{\lambda} \mathbf{a}_0 \otimes \mathbf{a}_0 + \bar{\lambda}^{-1/2} (\mathbf{I} - \mathbf{a}_0 \otimes \mathbf{a}_0) \\ &\text{with } (\mathbf{a}_0 \otimes \mathbf{a}_0)_{IJ} = \mathbf{a}_{0I} \times \mathbf{a}_{0J}, \end{aligned} \tag{3}$$

where $\bar{\lambda}$ is the macroscopic stretch along the fiber direction, and \mathbf{a}_0 is the fiber direction in the reference configuration (the symbol \otimes stands for the tensor product).

Due to the structure and deformation mechanisms of the fibrils, we assume that the plastic flow associates only with the uniaxial deformation of the fibrils, and the shear deformation of the fibrils is taken to be totally elastic. The uniaxial deformation gradient F_f can be further decomposed into elastic and plastic parts

$$F_f = F_f^e F_f^p, \tag{4}$$

where F_f^e and F_f^p represent the uniaxial elastic and plastic deformation along the fiber direction in the fibrils, respectively.

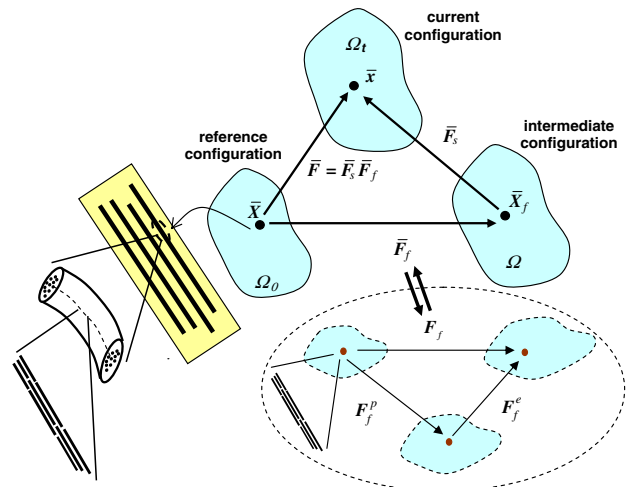


FIGURE 2. Multiplicative decomposition of the macroscopic deformation gradient of tissue.

From Eqs. (1), (2), and (4), we have

$$\bar{\mathbf{F}} = \bar{\mathbf{F}}^e \bar{\mathbf{F}}^p, \quad (5)$$

where $\bar{\mathbf{F}}^e = \bar{\mathbf{F}}_s \mathbf{F}_f^e$ and $\bar{\mathbf{F}}^p = \mathbf{F}_f^p$. The fiber direction in the current configuration is given by

$$\mathbf{a} = \frac{\bar{\mathbf{F}}\mathbf{a}_0}{\bar{\lambda}}, \quad (6)$$

where the macroscopic stretch is defined by $\bar{\lambda} = \sqrt{\bar{I}_4} = \sqrt{\bar{\mathbf{F}}\mathbf{a}_0 \cdot \bar{\mathbf{F}}\mathbf{a}_0}$.

Elastic Strain Energy of Fibrils and Plastic Flow Rule

We obtained the strain energy function of the tissue in a hierarchical way starting from the fibril response. Here the fibril is modeled as a generalized Neo-Hookean material characterized by the strain energy function¹²

$$\psi_{\text{fl}}^e(I_1^e, I_4^e) = \frac{\mu^{\text{fl}}(I_4^e)}{2}(I_1^e - 3), \quad (7)$$

where $I_1^e = \text{tr}(\mathbf{F}^e \mathbf{F}^{eT})$ with \mathbf{F}^e the elastic part of the deformation gradient of the fibrils, and $\mu^{\text{fl}} = \mu_0 f(I_4^e)$ with

$$f(I_4^e) = \tanh[a_1(I_4^e - 1)] + a_2 \exp[a_3(I_4^e - I_0)], \quad (8)$$

where a_1 , a_2 and a_3 are dimensionless material parameters, and μ_0 is the shear modulus of the fibril. The hyperbolic function in Eq. (8) characterizes the stiffness evolution of the fibrils embedded in crimped fibers during tissue stretching. It was experimentally observed that the collagen fibers in a relaxed tissue appear to be wavy and crimped.^{1,6} Thus, they sustain little load in the initial stage of the stretching of the tissue. This is reflected by the ‘‘toe’’ region of the tensile stress–strain curve of the tissue which is characterized by a small tangent modulus. Since the fibrils are embedded in the fiber being the major loading components, they should sustain little load before the crimped fiber is straightened. Furthermore, the material parameter I_0 in Eq. (8) is a critical value related to the secondary stiffening of the fibril. The secondary stiffening behavior of the fibril was revealed by Buehler⁴ through MD simulations. It was shown that there exists a second elastic regime characterized by an increased elastic modulus with increased fibril stretch for large cross-link densities. The fibrils generally fail prior to reaching the second elastic regime for smaller cross-link densities.

It is postulated that the plastic velocity gradient of the fibrils takes the deviatoric form¹⁰

$$\dot{\mathbf{F}}^p \mathbf{F}^{p-1} = \dot{\gamma} \text{dev}(\mathbf{a}_0 \otimes \mathbf{a}_0), \quad (9)$$

where $\dot{\gamma}$ is the plastic strain rate, and $\mathbf{F}^p = \mathbf{F}_f^p$ is the plastic part of the deformation gradient of the fibrils.

According to the assumption, there exists only uniaxial plastic deformation along the fibril direction which is volume-preserved. The plastic strain rate is assumed to take the power law form

$$\dot{\gamma} = \dot{\gamma}_0 \left| \frac{\Sigma_{\text{eff}}}{g} \right|^{1/m} \text{sign}(\Sigma_{\text{eff}}), \quad (10)$$

where

$$\Sigma_{\text{eff}} = \boldsymbol{\Sigma} : \text{dev}(\mathbf{a}_0 \otimes \mathbf{a}_0), \quad (11)$$

where $\boldsymbol{\Sigma} = \mathbf{F}^{eT} \boldsymbol{\tau} \mathbf{F}^{e-T}$ is the Mandel stress, and g is the flow resistance which evolves with time t in terms of

$$\dot{g}(t) = h \left(1 - \frac{g(t)}{g_s} \right) \dot{\gamma} \quad (12)$$

where g_s and h are the saturated flow strength and hardening or softening rate, respectively. Due to fibril softening associated with the breakage of cross links, the saturated flow strength, g_s , is generally chosen to be smaller than the initial yield strength of the fibril, g_0 , in the calculations here.

Buehler⁴ first introduced a parameter β describing the increase of adhesion at the ends of each TC molecule to reflect the variation of the cross-link densities. Experimental analyses of the molecular geometry suggests that intermolecular aldol cross-links between lysine or hydroxylysine residues, effectively leading to an increased adhesion between neighboring tropocollagen molecules at the location of cross-links, which primarily develop at the ends of tropocollagen molecules. The aldol cross-link is a C–C bond that forms between side chains of residues of two tropocollagen molecules. The parameter β describes the relative strength of the intermolecular adhesion, compared with a reference value that relates to non-covalent intermolecular interactions (e.g. H-bonds, vdW, Coulomb forces, etc.) that are present without cross-links. For a choice of $\beta = 12.5$, the additional shear force exerted at the end of the molecule corresponds to ≈ 4.2 nN, which is on the order of the bond strength of covalent cross-link bonds. The parameter $\beta = 12.5$ therefore corresponds to the case when approximately one cross link is present at each end of a tropocollagen molecule, leading to a cross-link density of $2.2 \times 10^{24}/\text{m}^3$ (the cross-link density is defined as the number of cross-links per unit volume). Similarly, doubling the value $\beta = 25$ corresponds to two covalent cross-links.

Through MD simulations,⁴ it was shown that the initial yield strength of the fibril, g_0 , strongly depends on β . In Fig. 3, the relationship of cross link parameter, β , and the initial yield strength of the fibril is illustrated. A function describing the variation of the initial yield strength with β is taken to have the form

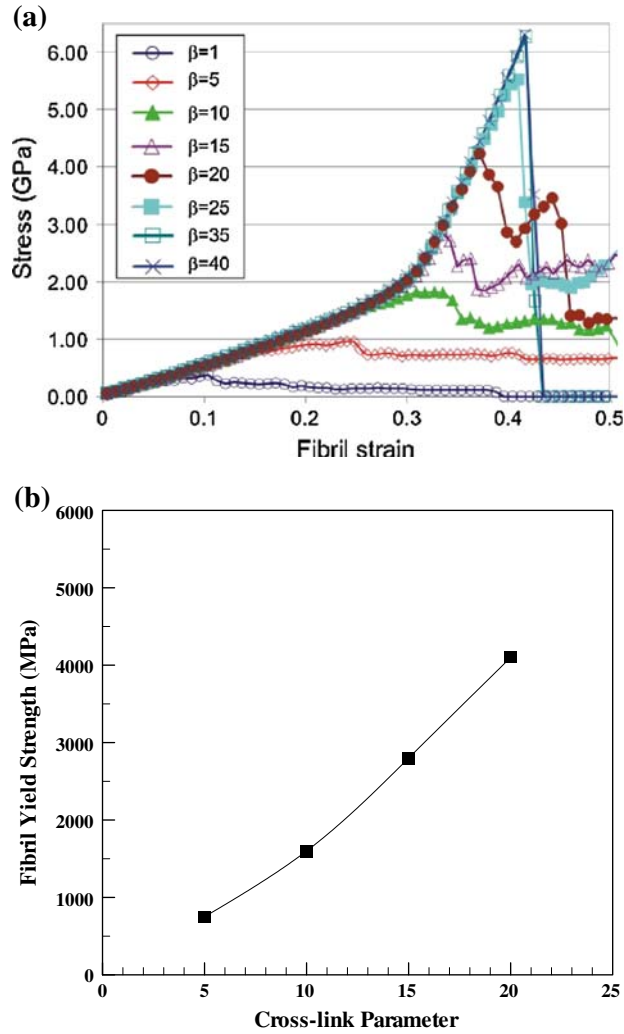


FIGURE 3. Initial yield strength of the fibril as a function of the cross-link parameter. Subplot (a) shows the original molecular dynamics results of the stress-strain behavior as a function of the cross-link parameter β ,⁴ and Subplot (b) depicts the analysis of the fibril yield strength as a function of the cross-link parameter β . The parameter $\beta = 12.5$ corresponds to the case when approximately one cross link is present at each end of a tropocollagen molecule, leading to a cross-link density of $2.2 \times 10^{24}/\text{m}^3$.

$$g_0(\beta) = g_i + c\beta^2, \quad (13)$$

where g_i is the yield strength of the fibril without cross-link, and c is a material constant. This relationship between yield strength and cross-link parameter β serves as the basis for the multi-scale coupling via parameter passing.

Elastic Strain Energy Function of Fiber

Here the fiber is considered as a composite reinforced by continuous fibrils as described in Fig. 4. The

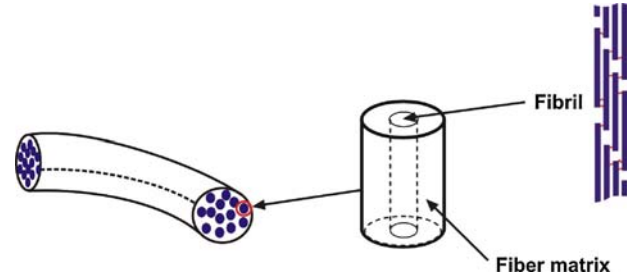


FIGURE 4. A representative volume element of the fiber.

matrix material of the fiber is modeled as an incompressible Neo-Hookean material characterized by the strain energy function

$$\psi_{\text{fm}}^e(I_1) = \frac{\mu^{\text{fm}}}{2}(I_1 - 3), \quad (14)$$

where μ^{fm} is the shear modulus of the fiber matrix material. The elastic strain energy density of the fiber under extension is given by

$$\psi_f^e(I_4, I_4^e) = v^{\text{fl}}\psi_{\text{fl}}^e(I_1(\mathbf{F}_f^e), I_4^e) + v^{\text{fm}}\psi_{\text{fm}}^e(I_1(\mathbf{F}_f)), \quad (15)$$

where $I_1(\mathbf{F}_f^e) = I_4^e + 2(I_4^e)^{-1/2}$, $I_1(\mathbf{F}_f) = I_4 + 2I_4^{-1/2}$, v^{fl} is the fibril volume fraction of the fiber, and $v^{\text{fm}} = 1 - v^{\text{fl}}$ is the volume fraction of the matrix material of the fiber. It is noted that $I_4 = \sqrt{\mathbf{F}_f \mathbf{a}_0 \cdot \mathbf{F}_f \mathbf{a}_0} = \bar{I}_4$.

The elastic strain energy function for the fiber under shear is given by

$$\psi_s^e(\bar{I}_1^{\text{fb}}, I_4, I_4^e) = \frac{\mu_{\text{eff}}^{\text{fb}}}{2} [\bar{I}_1^{\text{fb}} - I_1(\mathbf{F}_f)], \quad (16)$$

where^{2,12}

$$\mu_{\text{eff}}^{\text{fb}} = \mu^{\text{fm}} \frac{(1 + v^{\text{fl}})f(I_4^e) + (1 - v^{\text{fl}})}{(1 - v^{\text{fl}})f(I_4^e) + (1 + v^{\text{fl}})}, \quad (17)$$

and $\bar{I}_1^{\text{fb}} = \text{tr}(\bar{\mathbf{F}}_{\text{fiber}}^T \bar{\mathbf{F}}_{\text{fiber}})$ with $\bar{\mathbf{F}}_{\text{fiber}}$ the macroscopic deformation gradient of the fiber which is essentially a fibril-reinforced composite. The effective shear modulus as defined in Eq. (17) involves the effects of shear interactions at the interface of the fibril and matrix. The interaction at the interface of the matrix and fibers was also accounted for in the transversely isotropic hyperelastic model developed by Peng *et al.*²⁰ for the human annulus fibrosus. The total elastic strain energy density of the fiber includes the individual contributions due to the extension along the fibril direction and the remaining shear deformation. The strain energy function of the fiber is therefore written as

$$\psi_{\text{fb}}^e(\bar{I}_1^{\text{fb}}, I_4, I_4^e) = \psi_f^e(I_4, I_4^e) + \psi_s^e(\bar{I}_1^{\text{fb}}, I_4, I_4^e). \quad (18)$$

*Elastic Strain Energy of Tissue and Macroscopic
Constitutive Descriptions*

In Fig. 5, a representative cylindrical element of tissue is described. The tissue is treated as a fiber-reinforced composite. The elastic strain energy function of the matrix material of the tissue is taken to have the form

$$\psi_m^e(I_1) = \frac{\mu^m}{2}(I_1 - 3), \quad (19)$$

where μ^m is the shear modulus of the tissue matrix material. The elastic strain energy density of the tissue under extension is given by

$$\bar{\psi}_f^e(\bar{I}_4, \bar{I}_4^e) = v^f \psi_f^e(\bar{I}_4, \bar{I}_4^e) + v^m \psi_m^e(\bar{I}_1(\mathbf{F}_f)), \quad (20)$$

where v^f is the fiber volume fraction of the tissue, and $v^m = 1 - v^f$ is the volume fraction of the matrix of the tissue.

The elastic strain energy function of the tissue under shear is given by

$$\bar{\psi}_s^e(\bar{I}_1, \bar{I}_4, \bar{I}_4^e) = \frac{\mu_{\text{eff}}}{2}[\bar{I}_1 - \bar{I}_1(\mathbf{F}_f)], \quad (21)$$

where $\bar{I}_1 = \text{tr}(\bar{\mathbf{F}}^T \bar{\mathbf{F}})$ and

$$\mu_{\text{eff}} = \mu^m \frac{(1 + v^f)\mu_{\text{eff}}^{\text{fb}} + (1 - v^f)\mu^m}{(1 - v^f)\mu_{\text{eff}}^{\text{fb}} + (1 + v^f)\mu^m}. \quad (22)$$

The total elastic strain energy function of the tissue is defined by

$$\bar{\psi}^e(\bar{I}_1, \bar{I}_4, \bar{I}_4^e) = \bar{\psi}_f^e(\bar{I}_4, \bar{I}_4^e) + \bar{\psi}_s^e(\bar{I}_1, \bar{I}_4, \bar{I}_4^e). \quad (23)$$

A noticeable feature of the strain-energy function is that it depends on not only the elastic stretch but also the total deformation. This arises from the assumption made in developing the composite model that the plastic deformation only occurs in the fibril while the matrix materials always remain elastic. In the sense, the model is therefore quite different from the conventional

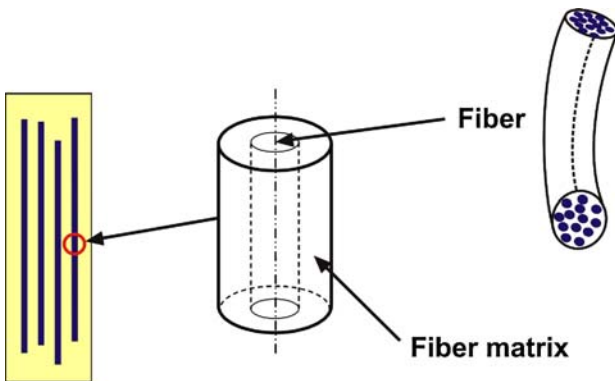


FIGURE 5. A representative volume element of the tissue.

hyperelasto-plastic model used for metallic crystalline materials. We can further write the strain-energy function of the tissue as

$$\begin{aligned} \bar{\psi}^e(\bar{I}_1, \bar{I}_4, \bar{I}_4^e) &= \frac{1}{2} \bar{\mu}^m (\bar{I}_4 + 2\bar{I}_4^{-1/2} - 3) \\ &+ \frac{1}{2} \bar{\mu}^{\text{fl}} (\bar{I}_4^e + 2\bar{I}_4^{e-1/2} - 3) \\ &+ \frac{\mu_{\text{eff}}}{2} [\bar{I}_1 - \bar{I}_1(\mathbf{F}_f)], \end{aligned} \quad (24)$$

where $\bar{\mu}_m = v^f v^{\text{fm}} \mu^{\text{fm}} + v^m \mu^m$, and $\bar{\mu}^{\text{fl}} = v^f v^{\text{fl}} \mu^{\text{fl}}$.

For an isothermal process, the Clausius–Duhem dissipation inequality at the macroscopic continuum level takes the form

$$\bar{\boldsymbol{\tau}} : \bar{\mathbf{d}} - \dot{\bar{\psi}}^e(\bar{I}_1, \bar{I}_4, \bar{I}_4^e) \geq 0, \quad (25)$$

where $\bar{\boldsymbol{\tau}}$ is the macroscopic Kirchhoff stress of the tissue continuum and $\bar{\mathbf{d}}$ is the macroscopic rate of deformation. Equation (25) is further written as

$$\left\{ \bar{\boldsymbol{\tau}} - \left(2 \frac{\partial \bar{\psi}^e}{\partial \bar{I}_1} \bar{\mathbf{b}} + 2\bar{I}_4 \frac{\partial \bar{\psi}^e}{\partial \bar{I}_4} \mathbf{a} \otimes \mathbf{a} + 2\bar{I}_4^e \frac{\partial \bar{\psi}^e}{\partial \bar{I}_4^e} \mathbf{a}^e \otimes \mathbf{a}^e \right) \right\} : \bar{\mathbf{d}} + 2\bar{I}_4^e \frac{\partial \bar{\psi}^e}{\partial \bar{I}_4^e} \mathbf{a}^e \otimes \mathbf{a}^e : \bar{\mathbf{d}}^p \geq 0, \quad (26)$$

where $\bar{\mathbf{d}}^p = \text{sym}(\bar{\mathbf{F}}^e \dot{\bar{\mathbf{F}}}^p \bar{\mathbf{F}}^{p-1} \bar{\mathbf{F}}^{e-1})$. Due to the material incompressibility of soft tissue, we have $\bar{J} = \det \bar{\mathbf{C}} = 1$ throughout the deformation. Thus, the required constraint on $\dot{\bar{\mathbf{C}}}$ is

$$\dot{\bar{J}} = \bar{J} \bar{\mathbf{C}}^{-1} : \dot{\bar{\mathbf{C}}} = 0. \quad (27)$$

To satisfy both the inequality (26) and the constraint condition (27), we have

$$\bar{\boldsymbol{\tau}} = 2 \frac{\partial \bar{\psi}^e}{\partial \bar{I}_1} \bar{\mathbf{b}} + 2\bar{I}_4 \frac{\partial \bar{\psi}^e}{\partial \bar{I}_4} \mathbf{a} \otimes \mathbf{a} + 2\bar{I}_4^e \frac{\partial \bar{\psi}^e}{\partial \bar{I}_4^e} \mathbf{a}^e \otimes \mathbf{a}^e - p \mathbf{I}, \quad (28)$$

and

$$2\bar{I}_4^e \frac{\partial \bar{\psi}^e}{\partial \bar{I}_4^e} \mathbf{a}^e \otimes \mathbf{a}^e : \bar{\mathbf{d}}^p \geq 0. \quad (29)$$

Equation (29) is further written as

$$\bar{\mathbf{F}}^{eT} \left(2\bar{I}_4^e \frac{\partial \bar{\psi}^e}{\partial \bar{I}_4^e} \mathbf{a}^e \otimes \mathbf{a}^e \right) \bar{\mathbf{F}}^{e-T} : \dot{\gamma} \text{dev}(\mathbf{a}_0 \otimes \mathbf{a}_0) \geq 0. \quad (30)$$

We can show that the inequality is equivalent to

$$\bar{\mathbf{F}}^{eT} \left(2\bar{I}_4^e \frac{\partial \bar{\psi}_s^e}{\partial \bar{I}_4^e} \mathbf{a}^e \otimes \mathbf{a}^e \right) \bar{\mathbf{F}}^{e-T} : \dot{\gamma} \text{dev}(\mathbf{a}_0 \otimes \mathbf{a}_0) \geq 0. \quad (31)$$

Note that the strain energy under shear, $\bar{\psi}_s^e$, is also functionally dependent on \bar{I}_4^e through the effective shear modulus. However, its contribution to the plastic

dissipation is neglected here. Macroscopically, the evolution of plastic strain in the fibril can be written as

$$\dot{\gamma} = \dot{\gamma}_0 \left| \frac{\bar{\Sigma}_{\text{eff}}}{g} \right|^{1/m} \text{sign}(\bar{\Sigma}_{\text{eff}}) \quad (32)$$

where

$$\bar{\Sigma}_{\text{eff}} = \bar{\Sigma} : \text{dev}(\mathbf{a}_0 \otimes \mathbf{a}_0), \quad (33)$$

and where

$$\bar{\Sigma} = \bar{\mathbf{F}}^{\text{eT}} \left(2\bar{I}_4^{\text{e}} \frac{\partial \psi_{\text{fl}}^{\text{e}}}{\partial \bar{I}_4^{\text{e}}} \mathbf{a}^{\text{e}} \otimes \mathbf{a}^{\text{e}} \right) \bar{\mathbf{F}}^{\text{e-T}} \quad (34)$$

is the macroscopic Mandel stress driving the plastic flow in the fibrils. Combining Eqs. (33) and (34), it is readily shown that the effective stress takes the form

$$\bar{\Sigma}_{\text{eff}} = \frac{4}{3} \bar{I}_4^{\text{e}} \frac{\partial \psi_{\text{fl}}^{\text{e}}}{\partial \bar{I}_4^{\text{e}}}. \quad (35)$$

In order to avoid numerical complications in the finite element implementation of an incompressible material model, we decouple the material response of the tissue into deviatoric and dilatational parts.²⁴ The reader is referred to Appendices A and B for an explicit derivation of the constitutive equations associated with the decoupled material response and the numerical integration procedure, respectively.

RESULTS AND DISCUSSIONS

Unless otherwise specified, the values of the material parameters used to characterize the continuum tissue model are summarized in Table 1. The shear modulus for the fibril, μ_0 , the critical stretch I_{cr} , and m were obtained by fitting the continuum fibril response to those predicted from MD simulations. The shear modulus for matrix material takes a much smaller value of 1.0 MPa which is on the order of magnitude used in Guo *et al.*¹² A low volume fraction is used for both fibril and fiber which is consistent with the typical volume fraction of collagen in tissue.

Material Response in Biaxial Stress

We first investigate the predictive capability of the present model under biaxial loading conditions as

TABLE 1. Parameters characterizing the tissue model.

v^{fl}	v^{f}	μ^{flm} (MPa)	μ^{m} (MPa)	μ_0 (MPa)	$\dot{\gamma}_0$ (s ⁻¹)	m	l_0
0.2	0.15	1.0	1.0	2000	0.01	0.05	2.4

illustrated in Fig. 6. It is assumed that the specimen has an arbitrary in-plane fiber direction $\mathbf{a} = \cos \alpha \mathbf{e}_1 + \sin \alpha \mathbf{e}_2$ where \mathbf{e}_i ($i = 1, 2$) is the Cartesian basis vectors, and α is the angle between the fiber direction and \mathbf{e}_1 . The deformation is driven by

$$\mathbf{F}(t) = \lambda(t) \mathbf{e}_1 \otimes \mathbf{e}_1 + \omega \lambda(t) \mathbf{e}_2 \otimes \mathbf{e}_2 + \frac{1}{\omega \lambda^2(t)} \mathbf{e}_3 \otimes \mathbf{e}_3, \quad (36)$$

where ω is a constant defining the stretch ratio of the x_1 and x_2 directions. Noting that the pressure p can be determined from the condition that $\sigma_3 = 0$, the stresses in the x_1 and x_2 directions are expressed as

$$\begin{aligned} \sigma_1 &= 2 \frac{\partial \bar{\psi}^{\text{e}}}{\partial \bar{I}_1} \left(\lambda^2 - \frac{1}{\omega^2 \lambda^4} \right) + 2 \frac{\partial \bar{\psi}^{\text{e}}}{\partial \bar{I}_4} \lambda^2 \cos^2 \alpha \\ &\quad + 2 \frac{\partial \bar{\psi}^{\text{e}}}{\partial \bar{I}_4} \lambda_e^2 \cos^2 \alpha \\ \sigma_2 &= 2 \frac{\partial \bar{\psi}^{\text{e}}}{\partial \bar{I}_1} \left(\omega^2 \lambda^2 - \frac{1}{\omega^2 \lambda^4} \right) + 2 \frac{\partial \bar{\psi}^{\text{e}}}{\partial \bar{I}_4} \omega^2 \lambda^2 \sin^2 \alpha \\ &\quad + 2 \frac{\partial \bar{\psi}^{\text{e}}}{\partial \bar{I}_4} \lambda_e^2 \sin^2 \alpha. \end{aligned} \quad (37)$$

For a rate-independent limit $m = 0$, the yielding condition can be expressed as

$$\bar{\Sigma}_{\text{eff}}(\bar{I}_4^{\text{e}}) = g_0, \quad (38)$$

where the effective stress, $\bar{\Sigma}_{\text{eff}}$, is defined by Eq. (35). By solving Eq. (35), a critical value I_{cr} can be determined such that the yielding occurs when $\bar{I}_4 = I_{\text{cr}}$.

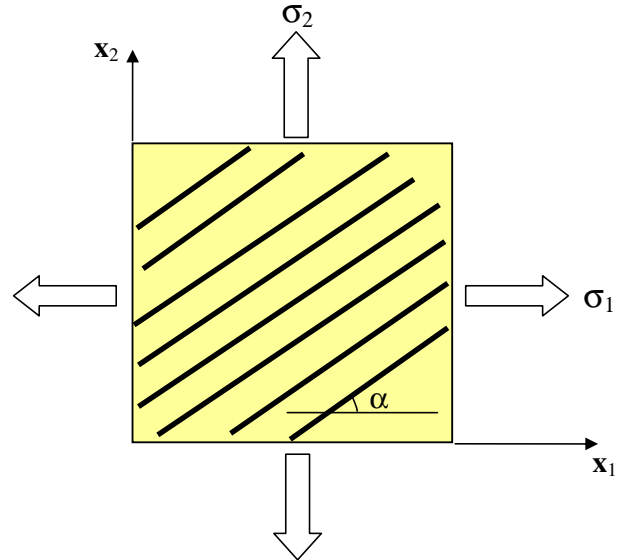


FIGURE 6. A tissue element subjected to biaxial stretches in the x_1 and x_2 directions. The fiber is oriented at α about the x_1 .

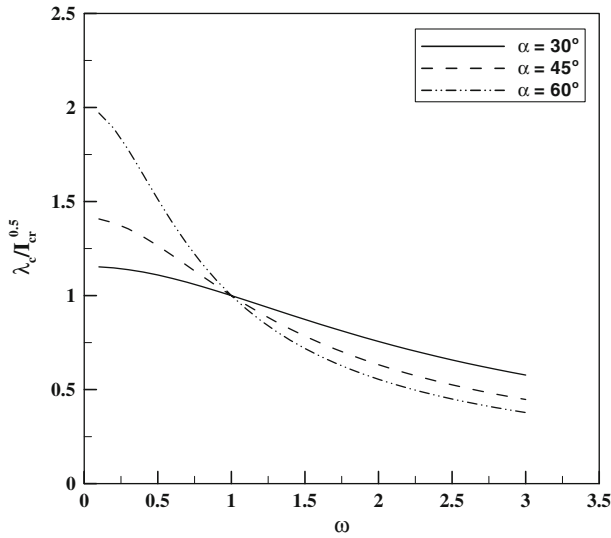


FIGURE 7. Critical stretch at which yielding occurs as a function of ω at varying fiber orientations.

Note that I_{cr} is a material constant independent of the loading conditions and fiber orientations. For the biaxial loading condition, we have

$$\bar{I}_4 = \lambda^2 \cos^2 \alpha + \omega^2 \lambda^2 \sin^2 \alpha. \quad (39)$$

It is readily shown that the critical stretch at which the yielding occurs is defined by

$$\lambda_c = \sqrt{\frac{I_{cr}}{\cos^2 \alpha + \omega^2 \sin^2 \alpha}}. \quad (40)$$

The critical stretch λ_c is not a material constant and its dependence on both the fiber orientation and ω is illustrated in Fig. 7. It is, however, noted that the critical stretch $\lambda_c = \sqrt{I_{cr}}$ which is independent of the fiber orientations for equal-biaxial loading $\omega = 1.0$.

We now proceed to investigate the stress–strain responses depending on both the fiber orientations and ω . In these calculations, the hardening rate is taken to be zero. In Fig. 8, we compare the stress–strain curves for different values of ω . The initial fiber direction is fixed at 45° about the x_1 axis. As we can see, the critical strain at which the yielding occurs increases with decreasing ω . This is consistent with Eq. (40). For $\omega = 2.0$, the fibers tend to be aligned with x_2 axis leading to the softening in the x_1 direction. In Figs. 9a–9c, the stress–strain curves for different fiber orientations are compared. The proportion constant ω takes a value of 0.5, 1.0, and 2.0 in Figs. 9a–9c, respectively. As shown in these figures, the material response in the x_1 direction becomes harder with decreasing α , while the critical strain at which the yielding occurs also depends on ω .

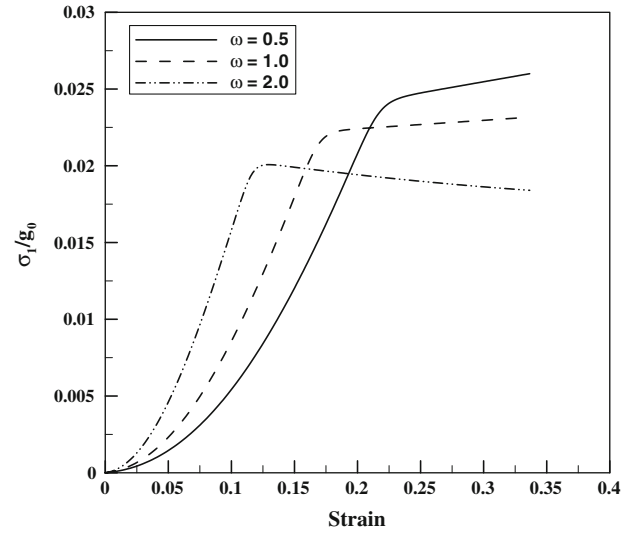


FIGURE 8. Comparison of stress–strain curves for different values of ω . The fiber is oriented in a 45° direction about the x_1 axis.

Tissue Response Dominated by the Fibril Behavior

According to the proposed tissue model, the inelastic deformation occurs only in the fibrils. The fibril composed of collagen molecules connected by cross-links is stiff and strong. The MD simulations reveal that the fibril has both the yield strength and stiffness on the order of 1–10 GPa. For the biological tissue, both the strength and stiffness are at least one order of magnitude smaller than those for the fibril. For example, the ultimate tensile strength for both ligament and tendon ranges from 50 to 100 MPa. The vast difference between the tissue and fibril strengths is due, in part, to the volume fraction of collagens and the composite structure of the tissue. The multi-scale modeling proposed in the present study is intended to help gain a better understanding of the structure-related mechanical behavior of soft tissue. This can play a significant role in tissue engineering for the creation of synthetic tissue to replace or repair portions of load-carrying soft tissue.

In Figs. 10–12, the tensile stress–strain behaviors of the fibril, fiber and tissue at different fibril yield strengths are displayed. This gives us a clear view on how the mechanical behavior of the tissue is dependant on the behavior of the fibril and fiber. The fibril yield strength typically increases with increasing density of the intermolecular cross links. In Fig. 10, the tensile stress–strain curves of the fibril for three cases $g_0 = 1200, 1800,$ and 3000 MPa are compared. Unless otherwise specified, the ratios $g_0/g_s = 6.0$ and $g_0/h = 1.0$ are held fixed. By using these parameters, we assume that the resistance to the deformation of the fibril decreases with increasing inelastic deformation. This can be due to the breakage of

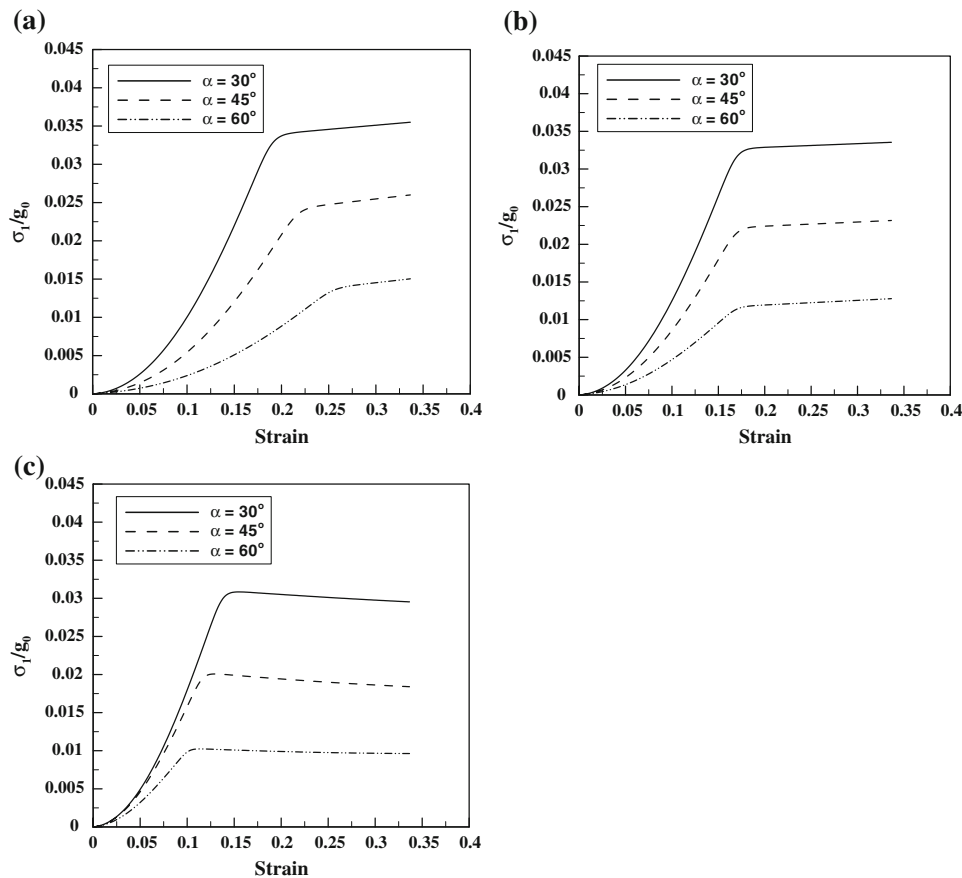


FIGURE 9. Comparison of stress–strain curves for different fiber orientations in cases (a) $\omega = 0.5$; (b) $\omega = 1.0$; and (c) $\omega = 2.0$.

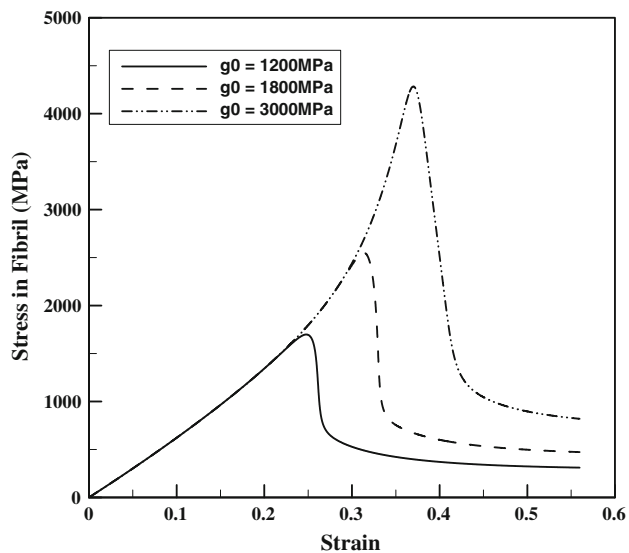


FIGURE 10. Stress–strain curves for the fibrils at varying initial flow strengths.

intermolecular cross-links. As shown in Fig. 10, significant load drops are exhibited due to a large softening rate in the calculations.

The fibers in the unloaded soft tissues were observed to display a crimped morphology. As a result, the fibers can be extended significantly with little load until they are straightened. This explains the “toe” region as exhibited in the typical tensile stress–strain behavior of tissue. By using the hyperbolic function as described in Eq. (8), the typical mechanical behavior of the crimped fibers can be well simulated. In Fig. 11, we show the predicted tensile stress–strain curves for the crimped fibers at different fibril yield strengths. As shown in this figure, three regions before fiber failure can be well identified in the tensile stress–strain curves. The toe region is characterized by a small tangent modulus. At the end of the toe region there is a gradual transition into the linear region of the stress–strain curve. Failure occurs near the end of the linear region.

The tensile behavior of tissues such as ligaments and tendons is dominated by the fibril behavior, since the fibrils are the major load-carrying components of the tissue under tension. In Fig. 12b, we show that the predicted macroscopic stress–strain curves of the tissue are similar to those for the fibers as described in Fig. 11. This is mainly attributed to the loading direction which is aligned with the fiber direction.

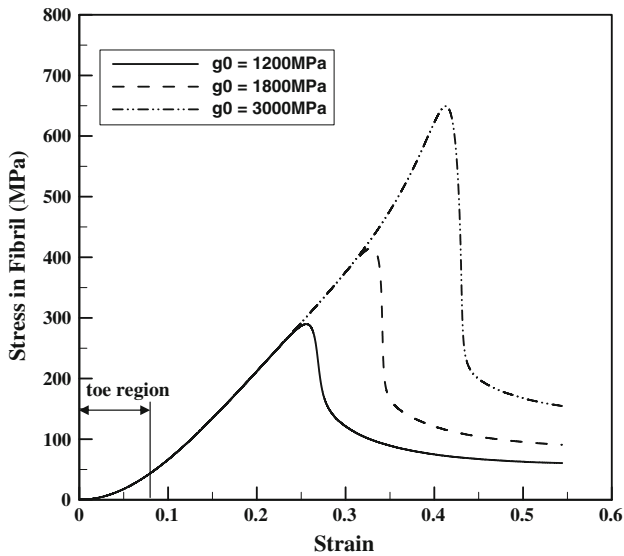


FIGURE 11. Stress–strain curves for the crimped fibers.

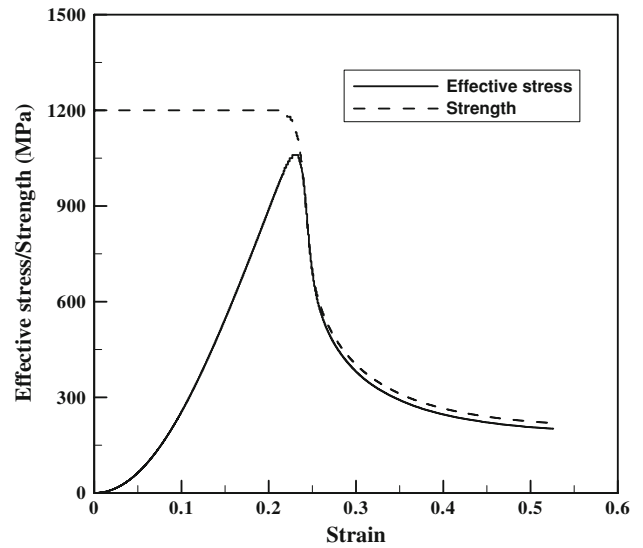


FIGURE 13. Evolution of the fibril strength and effective stress with tissue stretching.

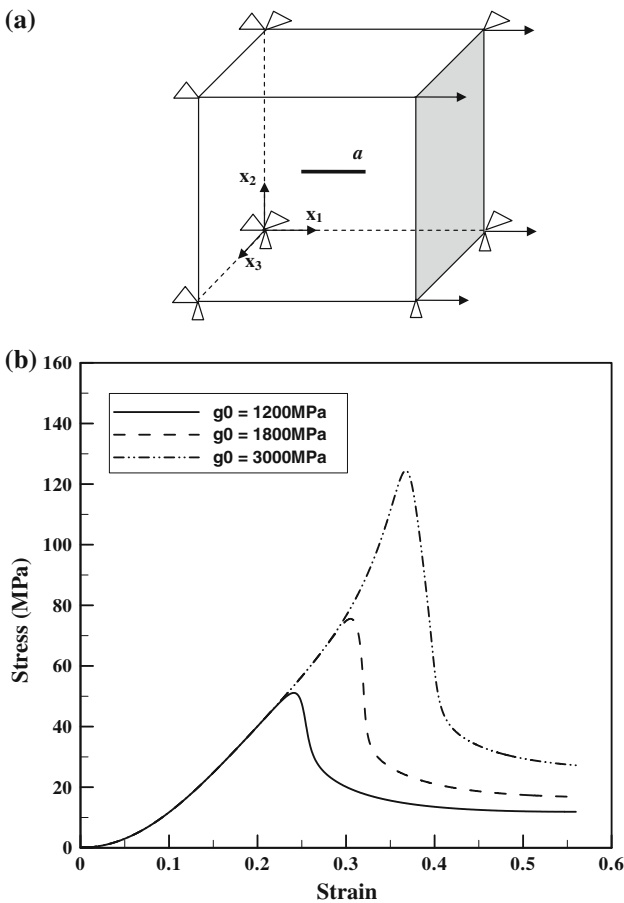


FIGURE 12. (a) Uniaxial unconstrained tension in the fiber direction of a tissue element. (b) Macroscopic stress–strain curves for the tissue at varying initial yield strengths (g_0 , which depends strongly on the cross-link density parameter β).

The simulations were conducted on a single block element as described in Fig. 12a. The stress–strain behaviors described in Fig. 12b therefore represent the mechanical response of a material point of the tissue or local response. It is noted that the overall tensile response of a tissue specimen can be very different from the local response especially in the presence of deformation localization associated with material instability. A comparison of the tissue response and fiber response clearly reveal that the macroscopic flow strength of the tissue is much smaller than that for the fiber, while the critical strain at which the failure occurs is almost the same as that for the fiber.

The significant load drop shown in the tensile stress–strain curves of the tissue is due to the decrease of the fibril strength with increasing inelastic deformation. In Fig. 13, the evolution of the fibril strength with tissue stretching is described. The initial yield strength of the fibril is 1200 MPa. The fibril resistance to the deformation starts decreasing as the effective stress in the fibril reaches a critical value with increasing tissue stretching. It is noted that the matrix materials of the tissue always remain elastic. Therefore, the resistance of the matrix materials keeps increasing with the deformation of the tissue. However, the overall response of the tissue exhibits significant softening as shown in Fig. 13, since its behavior is dominated by the mechanical behavior of the fibril.

Anisotropic Mechanical Behavior of Tissue

Here we investigate the anisotropic mechanical behavior of the tissue by means of a simple model

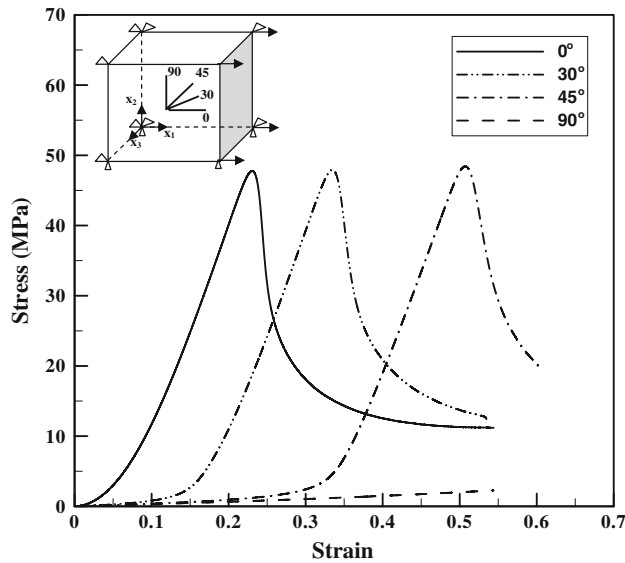


FIGURE 14. Dependence of the stress–strain response of the tissue on the fiber directions.

problem. A single cube reinforced by one family of fibers is considered. The cube is simulated by a single brick element as indicated in the inset of Fig. 14. The loading direction is fixed in the x_1 direction, while the fiber directions vary. The boundary conditions are employed such that the uniaxial tension is unconstrained. Four different fiber directions, 0° , 30° , 45° , and 90° about the x_1 direction are considered. In Fig. 14, the dependence of the tensile stress–strain response on the loading direction with respect to the fiber direction is revealed. As shown in this figure, for all fiber directions except the 90° direction (transverse loading), the material yielding followed by load drop occurs with increasing loading. With increasing angle between the fiber and loading directions, the critical strain for the occurrence of yielding increases. This is expected because the load sustained by the fibril decreases with increasing angle between the fiber and loading directions. During deformation, the fibers tend to be aligned with the loading direction for all these cases except the transverse loading case (90°). In the transverse loading case, the applied load is mainly sustained by the matrix material, and the fibers are not stretched. As a result, no material yielding is observed and the toe region is absent from the stress–strain curve. The stress level in this case is also significantly lower than that in the other cases.

Dependence of the Tissue Strength on the Cross-Link Parameter

The cross-link density of the fibril plays a significant role on its yield strength. The cross-link density can be

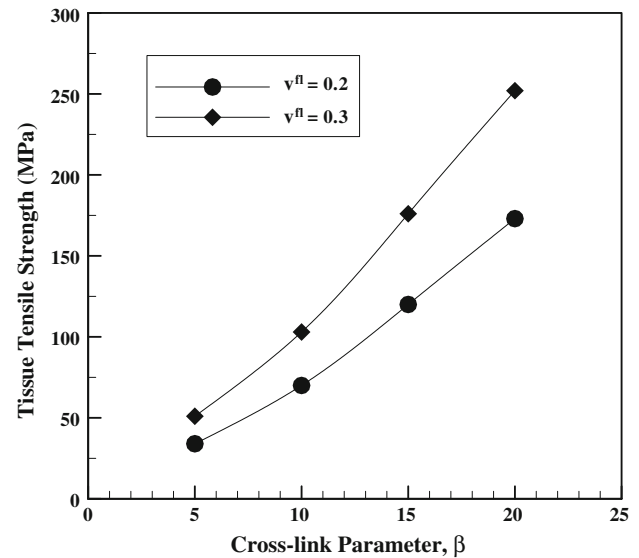


FIGURE 15. Tissue yield strength as a function of the cross-link parameter β for two different fibril volume fractions, $v^f = 0.2$ and $v^f = 0.3$.

characterized by the cross-link parameter, β , which describes the increase of adhesion at the ends of each TC molecule. In Fig. 3, we illustrate the relationship between the cross-link parameter and the fibril yield strength. By means of the proposed composite model, it is easy to determine the relationship between the tissue tensile strength and the cross-link parameter. The tensile strengths of the tissue as a function of the cross-link parameter β are described in Fig. 15. Here the tensile strength corresponds to the peak value in the tensile stress–strain curve of the tissue. As expected, the tissue strengths increase with increased value of β , following the same trend as that for the fibril.

The present model shows the potential of studying the effects of aging on the mechanical behavior of tissue. As we know, the cross-link densities generally increase with aging, thereby increasing the strength of fibrils.²³ The increase of the fibril strength may decrease the toughness of the fibril. From the present model, the tissue behavior can be obtained with known fibril properties. Therefore, we can know how the aging will influence the tissue behavior if the aging effects on the fibril behavior are known.

Localized Tensile Deformation in Large-Scale Tissue Continuum

The macroscopic response of a large-scale soft-tissue specimen under uniaxial tension is investigated in this section. The soft-tissue specimen submitted to uniaxial tension in the fiber direction (x_1 axis) is assumed to have plane-stress conditions. Due to the symmetries

about the middle planes, only one quadrant of the specimen is modeled. The initial length of the specimen is $2L$, and the width is $2W = 2L/3$. The finite element mesh of the model is described in Fig. 16.

Here we investigate the localization phenomenon induced by a small material inhomogeneity. In the calculations, the hardening rate is taken to be zero with $g_0 = g_s = 750$ MPa. The initial material inhomogeneity is imposed in a single element as indicated in Fig. 16 by taking a slightly smaller value of flow strength $g_0 = 748.5$ MPa. A material instability is expected to be initiated from this element. Three cases with the rate sensitivity $m = 0.005, 0.025, \text{ and } 0.05$ are considered.

In Figs. 17a–17c, the contours of Cauchy stress σ_{11} for the case $m = 0.005$ are described showing the development of plastic localization in the soft-tissue specimen. As shown in Fig. 17a, the localization of plastic deformation is initiated from the element with slightly smaller flow strength in the presence of a material instability. Once the material instability starts, the localized plastic deformation develops into a tensile band inside which the tensile strain is extremely large.

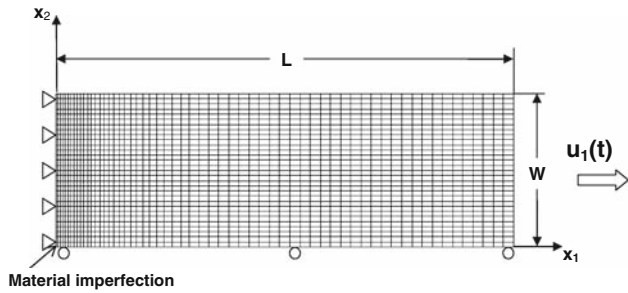


FIGURE 16. Finite element mesh of a soft-tissue specimen under uniaxial tension along the fiber direction.

The tensile band propagates rapidly through the cross-section of the tissue sheet once initiated. As described in Figs. 17b and 17c, the propagation of the tensile band is similar to that of a crack tip. Elastic unloading in the surrounding material of the tensile band is associated with its propagation. Figure 17 clearly display the expansion of the unloading region with the propagation of the tensile band. The released elastic energy due to the elastic unloading is mostly dissipated by the plastic deformation in the tensile band, thereby, facilitating its propagation. The force–displacement curve displayed in Fig. 18 shows that a sudden load

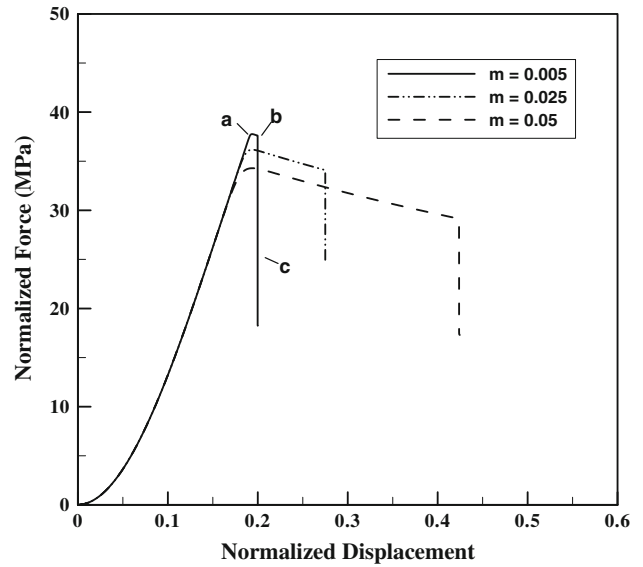


FIGURE 18. Dependence of tensile force–displacement responses on rate sensitivity. The corresponding distributions of tensile stress at the indicated points a, b and c are described in Figs. 17a–17c, respectively.

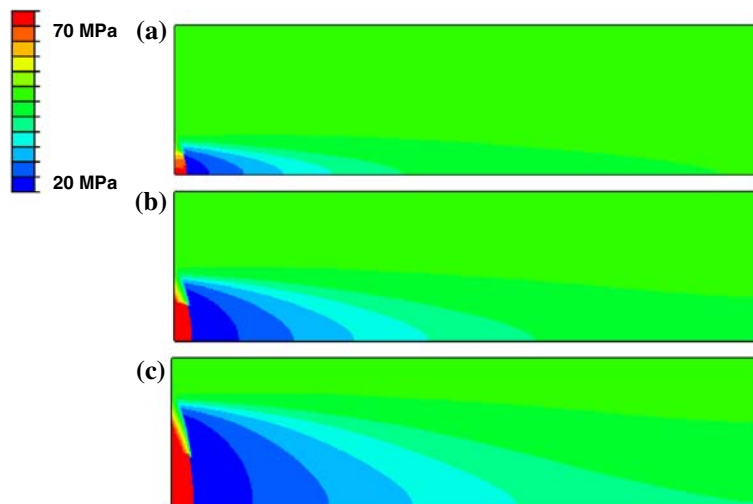


FIGURE 17. Distributions of tensile stress at (a) initiation of plastic localization, (b) early stage of the propagation of plastic localization and (c) final stage of plastic localization.

drop is associated with the propagation of the localized deformation. We note that the onset of material instabilities is not immediately associated with the load drop following the point of peak load. The small inhomogeneity initially grows slowly with plastic deformation until the onset of the material instability. As revealed in this figure, the onset of the material instability is significantly delayed for a large value of m , corresponding to strong material rate dependence. It is well known that material rate sensitivity plays a significant role in the development of shear bands in an elasto-viscoplastic material, for example, a ductile single crystal (Peirce *et al.*, 1983). An increase in material rate sensitivity can significantly retard the localization of plastic flow into an intensive deformation band, thereby, increasing the ductility of the material. This is consistent with our observations in Fig. 18.

Experimentally, it was shown that the tensile failure of soft tissue was typically associated with a steep load drop displayed in the measured load-displacement curve.²⁵ This is in good accord with the simulation results shown in Fig. 18. The present study shows that plastic localization can be an important mechanism leading to the failure of soft tissue. This is similar to shear localization occurring in metallic materials under tension which is the dominant failure mechanism. We believe that the present multi-scale constitutive model provides a powerful tool for helping better understand the failure and deformation mechanisms of soft tissue.

CONCLUDING REMARKS

In this study, a multi-scale constitutive model for soft tissue is developed. The deformation behavior of fibril on the nanoscale was obtained from MD simulations. The proposed constitutive model incorporates the deformation features of fibrils including both softening and secondary stiffening into a macroscopic constitutive description of the tissue continuum. The simulation results show that the model can capture the typical deformation behaviors of a soft tissue such as toe region displayed in the typical stress-strain curves, material anisotropy and softening beyond the physiological loading range. The multi-scale constitutive model takes into account the structure and deformation mechanisms of soft tissue. By means of this model, the macroscopic response of soft tissue can be directly linked to the cross link densities of fibrils. This can help understand the effects of aging on the human tissue behavior. A quantitative comparison between simulation and experimental measurements however needs to

be performed to further validate the proposed model. This will be conducted in future studies. An improved understanding of failure of biological tissues at multiple scales could enable tissue engineering approaches, the design of new biomaterials, and may also provide mechanistic insight into disease mechanisms.⁵

APPENDIX A: DECOUPLED VOLUMETRIC-DEVIATORIC RESPONSES

We write⁷

$$\tilde{\mathbf{F}} = \bar{J}^{-1/3} \bar{\mathbf{F}} = \bar{J}^{-1/3} \bar{\mathbf{F}}^e \bar{\mathbf{F}}^p, \quad (41)$$

where $\bar{J} = \det \bar{\mathbf{F}}$ and $\bar{\mathbf{F}}$ are associated with the volume-preserving macroscopic deformation. The plastic deformation is isochoric and the elastic part of $\bar{\mathbf{F}}$ is written as

$$\tilde{\mathbf{F}}^e = \bar{J}^{e-1/3} \bar{\mathbf{F}}^e, \quad (42)$$

where $\bar{J}^e = \bar{J}$. The right Cauchy-Green tensor associated with the deviatoric response is written as

$$\tilde{\mathbf{C}} = \tilde{\mathbf{F}}^T \tilde{\mathbf{F}}, \quad \tilde{\mathbf{C}}^e = \tilde{\mathbf{F}}^{eT} \tilde{\mathbf{F}}^e. \quad (43)$$

The corresponding invariants are defined as $\tilde{I}_1 = \text{tr}(\tilde{\mathbf{C}})$, $\tilde{I}_4 = \tilde{\mathbf{C}} : (\mathbf{a}_0 \otimes \mathbf{a}_0)$ and $\tilde{I}_4^e = \tilde{\mathbf{C}}^e : (\mathbf{a}_0 \otimes \mathbf{a}_0)$.

The total elastic strain energy function of the tissue is postulated to take the decoupled form

$$\Psi(\tilde{\mathbf{C}}, \tilde{\mathbf{C}}^e, \mathbf{a}_0 \otimes \mathbf{a}_0) = \bar{\psi}_{\text{iso}}^e(\tilde{I}_1, \tilde{I}_4, \tilde{I}_4^e) + \bar{\psi}_{\text{vol}}^e(\bar{J}), \quad (44)$$

where $\bar{\psi}_{\text{iso}}^e$ and $\bar{\psi}_{\text{vol}}^e$ are the isochoric and volumetric contributions to the material response of the tissue, respectively. The volumetric part of the total elastic strain energy is taken to be a convex function of \bar{J} with the form

$$\bar{\psi}_{\text{vol}}^e = \frac{\kappa}{2} (\bar{J} - 1)^2. \quad (45)$$

The isochoric part of the total elastic strain energy takes the form

$$\bar{\psi}_{\text{iso}}^e(\tilde{I}_1, \tilde{I}_4, \tilde{I}_4^e) = \bar{\psi}_f^e(\tilde{I}_4, \tilde{I}_4^e) + \bar{\psi}_s^e(\tilde{I}_1, \tilde{I}_4, \tilde{I}_4^e), \quad (46)$$

where, using Eqs. (15) and (20),

$$\begin{aligned} \bar{\psi}_f^e(\tilde{I}_4, \tilde{I}_4^e) &= v^f v^{\text{fl}} \psi_{\text{fl}}^e(\tilde{I}_1(\tilde{\mathbf{F}}_f^e), \tilde{I}_4^e) + v^f v^{\text{fm}} \psi_{\text{fm}}^e(\tilde{I}_1(\tilde{\mathbf{F}}_f)) \\ &\quad + v^m \psi_m^e(\tilde{I}_1(\tilde{\mathbf{F}}_f)), \end{aligned} \quad (47)$$

and

$$\bar{\psi}_s^e(\tilde{I}_1, \tilde{I}_4, \tilde{I}_4^e) = \frac{\tilde{\mu}_{\text{eff}}(\tilde{I}_4^e)}{2} [\tilde{I}_1 - \tilde{I}_1(\tilde{\mathbf{F}}_f)], \quad (48)$$

where $\tilde{I}_1(\tilde{\mathbf{F}}_f) = \tilde{I}_4 + 2(\tilde{I}_4)^{-1/2}$.

The second Piola–Kirchhoff stress is split into a purely volumetric contribution and a purely isochoric contribution with the form $\bar{\mathbf{S}} = \bar{\mathbf{S}}_{\text{vol}} + \bar{\mathbf{S}}_{\text{iso}}$. We have

$$\bar{\mathbf{S}}_{\text{iso}} = 2 \frac{\partial \bar{\psi}_{\text{iso}}^e(\tilde{I}_1, \tilde{I}_4, \tilde{I}_4^e)}{\partial \bar{\mathbf{C}}} + 2 \bar{\mathbf{F}}^{\text{p}-1} \frac{\partial \bar{\psi}_{\text{iso}}^e(\tilde{I}_1, \tilde{I}_4, \tilde{I}_4^e)}{\partial \bar{\mathbf{C}}^e} \bar{\mathbf{F}}^{\text{p}-\text{T}}, \quad (49)$$

noting the pull back of the stress from the intermediate configuration to the reference configuration in the third term of the equation. Equation (49) is further written as

$$\begin{aligned} \bar{\mathbf{S}}_{\text{iso}} &= \bar{J}^{-2/3 \text{p}} : \left(2 \frac{\partial \bar{\psi}_{\text{iso}}^e(\tilde{I}_1, \tilde{I}_4, \tilde{I}_4^e)}{\partial \bar{\mathbf{C}}} \right) \\ &\quad + \bar{\mathbf{F}}^{\text{p}-1} \bar{J}^{\text{e}-2/3 \text{pe}} : \left(2 \frac{\partial \bar{\psi}_{\text{iso}}^e(\tilde{I}_1, \tilde{I}_4, \tilde{I}_4^e)}{\partial \bar{\mathbf{C}}^e} \right) \bar{\mathbf{F}}^{\text{p}-\text{T}} \\ &= \bar{J}^{-2/3 \text{p}} : \left(2 \frac{\partial \bar{\psi}_{\text{iso}}^e(\tilde{I}_1, \tilde{I}_4, \tilde{I}_4^e)}{\partial \tilde{I}_1} \mathbf{I} \right. \\ &\quad \left. + 2 \frac{\partial \bar{\psi}_{\text{iso}}^e(\tilde{I}_1, \tilde{I}_4, \tilde{I}_4^e)}{\partial \tilde{I}_4} \mathbf{a}_0 \otimes \mathbf{a}_0 \right) + \bar{\mathbf{F}}^{\text{p}-1} \bar{J}^{\text{e}-2/3 \text{pe}} : \\ &\quad \left(2 \frac{\partial \bar{\psi}_{\text{iso}}^e(\tilde{I}_1, \tilde{I}_4, \tilde{I}_4^e)}{\partial \tilde{I}_4^e} \mathbf{a}_0 \otimes \mathbf{a}_0 \right) \bar{\mathbf{F}}^{\text{p}-\text{T}}, \quad (50) \end{aligned}$$

where

$$\mathbb{I} = \mathbb{I} - \frac{1}{3} \bar{\mathbf{C}}^{-1} \otimes \bar{\mathbf{C}} \text{ and } \mathbb{I}^{\text{e}} = \mathbb{I} - \frac{1}{3} \bar{\mathbf{C}}^{\text{e}-1} \otimes \bar{\mathbf{C}}^{\text{e}}, \quad (51)$$

with \mathbb{I} the fourth order identity tensor. The volumetric part of the second Piola–Kirchhoff stress takes the form

$$\bar{\mathbf{S}}_{\text{vol}} = \bar{J} \text{p} \bar{\mathbf{C}}^{-1} = \bar{J} \kappa (\bar{J} - 1) \bar{\mathbf{C}}^{-1}. \quad (52)$$

Combining Eqs. (50) and (52), the Kirchhoff stress is shown to have the form

$$\begin{aligned} \bar{\boldsymbol{\tau}} &= \bar{\mathbf{F}} \bar{\mathbf{S}} \bar{\mathbf{T}}^{\text{T}} = 2 \frac{\partial \bar{\psi}_{\text{iso}}^e(\tilde{I}_1, \tilde{I}_4, \tilde{I}_4^e)}{\partial \tilde{I}_1} \text{dev } \tilde{\mathbf{b}} \\ &\quad + 2 \tilde{I}_4 \frac{\partial \bar{\psi}_{\text{iso}}^e(\tilde{I}_1, \tilde{I}_4, \tilde{I}_4^e)}{\partial \tilde{I}_4} \text{dev}(\mathbf{a} \otimes \mathbf{a}) \\ &\quad + 2 \tilde{I}_4^e \frac{\partial \bar{\psi}_{\text{iso}}^e(\tilde{I}_1, \tilde{I}_4, \tilde{I}_4^e)}{\partial \tilde{I}_4^e} \text{dev}(\mathbf{a}^{\text{e}} \otimes \mathbf{a}^{\text{e}}) + \kappa \bar{J} (\bar{J} - 1) \mathbf{I}. \quad (53) \end{aligned}$$

APPENDIX B: TIME-INTEGRATION PROCEDURE

Given $\bar{\mathbf{F}}(t_{n+1})$ at time $t_{n+1} = t_n + \Delta t$, we need to find $\bar{\mathbf{F}}^{\text{e}}(t_{n+1})$ to determine the stress sustained by the fibril

in the current configuration. Based on the multiplicative decomposition, the elastic part of the deformation gradient is determined by

$$\bar{\mathbf{F}}_{n+1}^{\text{e}} = \bar{\mathbf{F}}_{n+1} \bar{\mathbf{F}}_{n+1}^{\text{p}-1}. \quad (54)$$

With the assumption $\bar{J} = \bar{J}^{\text{e}}$ and $\bar{J}^{\text{p}} = 1$, we have

$$\tilde{\mathbf{F}}_{n+1}^{\text{e}} = \tilde{\mathbf{F}}_{n+1} \bar{\mathbf{F}}_{n+1}^{\text{p}-1}. \quad (55)$$

By integrating Eq. (9), the plastic part of the deformation gradient at time t_{n+1} takes the form

$$\bar{\mathbf{F}}_{n+1}^{\text{p}} = \exp(\Delta t \dot{\gamma}_{n+1} \text{dev}(\mathbf{a}_0 \otimes \mathbf{a}_0)) \bar{\mathbf{F}}_n^{\text{p}}. \quad (56)$$

In the calculations here, we use the approximate form

$$\bar{\mathbf{F}}_{n+1}^{\text{p}} \doteq (\mathbf{I} + \Delta t \dot{\gamma}_{n+1} \text{dev}(\mathbf{a}_0 \otimes \mathbf{a}_0)) \bar{\mathbf{F}}_n^{\text{p}}, \quad (57)$$

which arises from a first order Taylor-series expansion of the exponential function as shown in Eq. (56). A simpler method is also used in the calculations conducted here. We write the plastic deformation gradient as

$$\bar{\mathbf{F}}^{\text{p}} = \lambda^{\text{p}} \mathbf{a}_0 \otimes \mathbf{a}_0 + \lambda^{\text{p}-1/2} (\mathbf{I} - \mathbf{a}_0 \otimes \mathbf{a}_0), \quad (58)$$

where λ^{p} is the plastic stretch along the fiber direction. Equation (58) reflects the incompressibility of plastic deformation and the nature of uniaxial plastic flow along the fiber direction. Combining Eqs. (58) and (9), we have

$$\frac{\dot{\lambda}^{\text{p}}}{\lambda^{\text{p}}} = \frac{2}{3} \dot{\gamma}. \quad (59)$$

Integrating Eq. (59), we have

$$\lambda^{\text{p}} = \exp\left(\frac{2}{3} \int \dot{\gamma} dt\right). \quad (60)$$

The plastic stretch at current time is updated as

$$\lambda_{t+\Delta t}^{\text{p}} = \lambda_t^{\text{p}} \exp\left(\frac{2}{3} \Delta \gamma_{t+\Delta t}\right), \quad (61)$$

where $\Delta \gamma_{t+\Delta t} = \dot{\gamma}_{t+\Delta t} \Delta t$. Unless otherwise specified, the variables without subscript represent the values at time $t_{n+1} = t_n + \Delta t$ in the following.

Now we need to find the plastic strain increment $\Delta \gamma = \Delta t \dot{\gamma}$ to determine the plastic part of the deformation gradient. This is realized by updating both the flow strength and the resolved Mandel stress along the fiber direction. According to a backward discretization of Eq. (12), the flow strength at current time is updated as

$$\mathbf{g} = \frac{h \Delta \gamma + \mathbf{g}_t}{1 + h \Delta \gamma / g_s}. \quad (62)$$

Here we define two coupled residual functions as

$$\begin{cases} R_1(\tilde{\Sigma}_{\text{eff}}, g) = \tilde{\Sigma}_{\text{eff}} - \frac{4}{3} \tilde{\gamma}_4^e \frac{\partial \Psi_{\text{fl}}^e}{\partial \tilde{I}_4^e} \\ R_2(\tilde{\Sigma}_{\text{eff}}, g) = g - \frac{h \Delta \gamma (\tilde{\Sigma}_{\text{eff}}, g) + g_t}{1 + h \Delta \gamma (\tilde{\Sigma}_{\text{eff}}, g) / g_s} \end{cases} \quad (63)$$

A general Newton–Raphson method is used to solve the coupled equations

$$\begin{cases} R_1(\tilde{\Sigma}_{\text{eff}}, g) = 0 \\ R_2(\tilde{\Sigma}_{\text{eff}}, g) = 0 \end{cases} \quad (64)$$

We have

$$\begin{bmatrix} \tilde{\Sigma}_{\text{eff}}^{k+1} \\ g^{k+1} \end{bmatrix} = \begin{bmatrix} \tilde{\Sigma}_{\text{eff}}^k \\ g^k \end{bmatrix} - (\mathbf{G}^k)^{-1} \cdot \begin{bmatrix} R_1^k \\ R_2^k \end{bmatrix}, \quad (65)$$

where

$$\mathbf{G}^k = \begin{bmatrix} \frac{\partial R_1}{\partial \tilde{\Sigma}_{\text{eff}}} & \frac{\partial R_1}{\partial g} \\ \frac{\partial R_2}{\partial \tilde{\Sigma}_{\text{eff}}} & \frac{\partial R_2}{\partial g} \end{bmatrix}^k \quad (66)$$

with k the iteration number.

ACKNOWLEDGMENTS

The authors state that they have no competing financial interests. Support was provided by a National Science Foundation CAREER Award (grant number CMMI-0642545), by the Army Research Office (grant number W911NF-06-1-0291), as well as the Air Force Office of Scientific Research.

REFERENCES

- ¹Baer, E., J. J. Cassidy, and A. Hiltner. Hierarchical structure of collagen composite systems: lessons from biology. *Pure Appl. Chem.* 63:961–973, 1991.
- ²deBotton, G., I. Hariton, and E. A. Socolsky. Neo-Hookean fiber-reinforced composites in finite elasticity. *J. Mech. Phys. Solids* 54:533–559, 2006.
- ³Buehler, M. J. Explaining the nanostructure of collagen fibrils. *Proc. Natl. Acad. Sci. U.S.A.* 103(33):12285–12290, 2006.
- ⁴Buehler, M. J. Nanomechanics of collagen fibrils under varying cross-link densities: atomistic and continuum studies. *J. Mech. Behav. Biomed. Mater.* 1(1):59–67, 2008.
- ⁵Buehler, M. J., and Y. C. Yung. Deformation and failure of protein materials in physiologically extreme conditions and disease. *Nat. Mater.* 8(3):1–14, 2009.
- ⁶Diamant, J., A. Keller, E. Baer, M. Litt, and R. G. C. Arridge. Collagen: ultrastructure and its relation to mechanical

- properties as a function of aging. *Proc. R. Soc. B: Biol. Sci.* 180:293–315, 1972.
- ⁷Flory, P. J. Thermodynamic relations for highly elastic materials. *Trans. Faraday Soc.* 57:829–838, 1961.
- ⁸Fratzl, P. Cellulose and collagen: from fibers to tissues. *Curr. Opin. Colloid Interf. Sci.* 8:32–39, 2003.
- ⁹Fung, Y. C. *Biomechanics-Mechanical Properties of Living Tissues*. 2nd ed. New York: Springer, 1993.
- ¹⁰Gasser, T. C., and G. A. Holzapfel. A rate-independent elastoplastic constitutive model for biological fiber-reinforced composites at finite strains: continuum basis, algorithmic formulation and finite element implementation. *Comput. Mech.* 29:340–360, 2002.
- ¹¹Guo, Z. Y., F. Caner, X. Q. Peng, and B. Moran. On constitutive modelling of porous neo-Hookean composites. *J. Mech. Phys. Solids* 56:2338–2357, 2008.
- ¹²Guo, Z. Y., X. Q. Peng, and B. Moran. A composites-based hyperelastic constitutive model for soft tissue with application to the human annulus fibrosus. *J. Mech. Phys. Solids* 54:1952–1971, 2006.
- ¹³Holzapfel, G. A. Biomechanics of soft tissue. In: *Handbook of Material Behavior: Nonlinear Models and Properties*, edited by J. Lemaitre and L. M. T. Cahan. Academic Press Inc., pp. 1–12, 2000; No. 7 in *Biomechanics Reprint Series*.
- ¹⁴Holzapfel, G. A. *Nonlinear Solid Mechanics: A Continuum Approach for Engineering*. Wiley, 2000.
- ¹⁵Holzapfel, G. A. Nonlinear solid mechanics: computational biomechanics of soft biological tissue. *Encyclopedia Comput. Mech.* 2:605–635, 2004.
- ¹⁶Kroon, M., and G. Holzapfel. A new constitutive model for multi-layered collagenous tissues. *J. Biomech.* 41:2766–2771, 2008.
- ¹⁷Limbirt, G., and J. Middleton. A constitutive model of the posterior cruciate ligament. *Med. Eng. Phys.* 28(2):99–113, 2006.
- ¹⁸Lubarda, V. A. *Elastoplasticity Theory*. CRC Press LLC, 2002.
- ¹⁹MacArthur, B. D., and R. O. C. Oreffo. Bridging the gap. *Nature* 433:19, 2005.
- ²⁰Peng, X. Q., Z. Y. Guo, and B. Moran. An anisotropic hyperelastic constitutive model with fiber–matrix shear interaction for the human annulus fibrosus. *J. Appl. Mech.* 73:815–824, 2006.
- ²¹Tanaka, E., and H. Yamada. An inelastic constitutive model of blood vessels. *Acta Mech.* 82:21–30, 1990.
- ²²Tanaka, E., H. Yamada, and S. Murakami. Inelastic constitutive modeling of arterial and ventricular walls. In: *Computational Biomechanics*, edited by K. Hayashi and H. Ishikawa. Tokyo: Springer-Verlag, pp. 137–163, 1996.
- ²³Tuite, D. J., P. A. F. H. Renstrom, and M. O’Brien. The aging tendon. *Scand. J. Med. Sci. Sports* 7:72–77, 1997.
- ²⁴Weiss, J. A., B. N. Maker, and S. Govindjee. Finite element implementation of incompressible transversely isotropic hyperelasticity. *Comput. Methods Appl. Mech. Eng.* 135:107–128, 1996.
- ²⁵Woo, S. L., M. Hollis, D. J. Adams, R. M. Lyon, and S. Taka. Tensile properties of the human femur-anterior cruciate ligament-tibia complex. *Am. J. Sports Med.* 19: 217–225, 1991.